JOURNAL OF Materials CHEMISTRY

Electrochemical properties of manganese vanadium molybdenum oxide as the anode for Li secondary batteries

D. Hara, H. Ikuta, Y. Uchimoto and M. Wakihara*

Department of Applied Chemistry, Graduate School of Science and Engineering, Tokyo Institute of Technology, 2-12-1, Okayama, Meguro-ku, Tokyo 152-8552, Japan. E-mail: mwakihar@o.cc.titech.ac.jp; Fax: +81 3 5734 2146; Tel: + 81 3 5734 2145

Received 27th February 2002, Accepted 31st May 2002
First published as an Advance Article on the web 1st July 2002

Solid solutions of $Mn_{1-x}Mo_{2x}V_{2(1-x)}O_6$ ($x = 0$, 0.4) were synthesized by classical solid-state reaction from Mn_2O_3, V_2O_5, and MoO_3 as starting materials. X-Ray diffraction (XRD) analysis showed that the prepared samples belong to the monoclinic brannerite-type structure with space group *C*2/*m*. *L*-Edge X-ray absorption near-edge structure (XANES) data of Mn, V and Mo in $Mn_{1-x}Mo_{2x}V_{2(1-x)}O_6$ ($x = 0$, 0.4) revealed that the valences of the corresponding metals are almost +2, +5 and +6, respectively. The electrochemical properties were considerably affected by Mo doping. The brannerite $Mn_{0.6}Mo_{0.8}V_{1.2}O_6$, which is an intermediate composition of $Mn_{1-x}Mo_{2x}V_{2(1-x)}O_6$, exhibited a higher charge–discharge capacity of 1000 Ah kg^{-1} and enhanced rate capabilities compared with the parent MnV_2O_6.

Introduction

In recent years, lithium ion batteries have received much attention because of their wide range of applications as the power source for portable telephones and laptop computers *etc.*[1,2] Generally, commercially available lithium ion batteries consist of two Li-intercalation materials as both cathode and anode materials. Commonly, lithiated transition metal oxides are used as the cathode and graphite is used as the anode. However, the graphite anode suffers from a low specific capacity (about 350 Ah kg^{-1}). Furthermore, the poor lithium ion diffusivity in graphite,[3] which is lower than that of $LiCoO_2$[4] or $LiMn_2O_4$,[5] limits charge–discharge rates. Hence, the capacity and the charge–discharge rate capability of graphite material need to be improved to attain much more capacity and rapid charge–discharge of the cell.

In order to overcome such problems of the graphite material, it is desired to synthesize novel anode materials with larger capacity and higher lithium ion diffusivity. Therefore, a considerable number of materials involving oxides,[6,7] nitrides[8,9] and intermetallics[10,11] have been studied as alternative anode materials. Among them, oxide anodes are attractive because of their chemical stability and high capacity. In a previous paper,[12] we proposed a novel oxide anode of MnV_2O_6 synthesized by a polymer gelation method. The MnV_2O_6 compound showed a monoclinic brannerite type structure with space group *C*2/*m*, and exhibited a reversible capacity of about 800 Ah kg^{-1} which is more than twice as large as that of graphite. Furthermore, the brannerite MnV_2O_6 compound had better rate capability than that of graphite.

In this study, we synthesized Mo doped MnV_2O_6 ($Mn_{1-x}Mo_{2x}V_{2(1-x)}O_6$ ($x = 0$, 0.4)) by conventional solid-state reaction and investigated its electrochemical properties as well. In the crystal structure of $Mn_{1-x}Mo_{2x}V_{2(1-x)}O_6$, Mn and Mn vacancies are randomly distributed over the original Mn sites, whereas V and Mo randomly occupy the original V sites in the parent MnV_2O_6.[13] Therefore, we expect that these vacancies on Mn sites might work effectively for Li ion diffusion, which would lead to a higher rate performance than that of an undoped sample. The charge–discharge cycle performance for $Mn_{1-x}Mo_{2x}V_{2(1-x)}O_6$ will be presented including the results of XRD and XANES measurements.

Experimental

The samples, $Mn_{1-x}Mo_{2x}V_{2(1-x)}O_6$ ($x = 0$, 0.4), were prepared by conventional solid-state reaction. The starting materials used were Mn_2O_3, V_2O_5 (99.9% Soekawa chemicals) and MoO_3 (99.9% Soekawa chemicals). Mn_2O_3 was prepared by pyrolysis of $MnCO_3$ (99.9% Soekawa chemicals) at 600 °C for 1 day in air atmosphere. The stoichiometric amounts of these materials were mixed and ground in an agate mortar. The resulting mixture was pressed into pellets and heated in air at 600 °C for 3 days with intermittent grindings, followed by slow cooling at a cooling rate of 1 °C min^{-1}. The phase identification and the evaluation of the lattice parameters of the prepared samples were carried out by powder X-ray diffractometry (XRD) using a Rigaku RINT2500V with CuKα radiation at room temperature. The XRD data for the determination of lattice parameters were collected in the 2θ range of 10–100°. In order to determine the oxidation states of Mn, V and Mo on the synthesized compounds, X-ray absorption near edge structure (XANES) measurements were performed. *L*-Edge XANES spectra were measured at UVSOR (Okazaki, Japan) with a ring energy of 750 MeV and a stored current of 70–220 mA in a mode of total electron yields at room temperature. The beam lines were BL8B1 for the Mn and V *L*-edges, and BL7A for the Mo *L*-edge. A KTP double crystal monochromator was used at BL7A. The absolute energy scales were calibrated by using literature values of Mn, V and Mo L_{III}-edges in Mn_2O_3,[14] V_2O_3[15] and MoO_3[16] respectively. *K*-Edge XANES measurements were performed at Photon Factory (PF, Tsukuba, Japan) with a ring energy of 2.5 GeV and a stored current of 440 mA in a mode of total electron yields at room temperature. The data were collected in transmission mode at the Mn and V *K*-edges on beam line BL9A, and the Mo *K*-edge on BL10B with double crystal monochromators of Si (111) and Si (311), respectively.

A CR2032 coin-type cell was selected for charge–discharge measurements. The working electrode was fabricated by the doctor-blade technique on a copper foil, the spreading paste consisted of 10 wt% polyvinylidenefluoride (PVDF) binder, 20 wt% acetylene black (conductive agent), 70 wt% active material of $Mn_{1-x}Mo_{2x}V_{2(1-x)}O_6$ ($x = 0$, 0.4) and appropriate amount of *N*-methyl-2-pyrrolidinone (NMP) as solvent.

The NMP solvent was evaporated in a furnace at 110 °C in air atmosphere for 1 day, and then the electrodes were roll-pressed and cut into disks. Lithium metal was used as a counter electrode. The electrolyte was 1 M $LiClO_4$ dissolved in ethylene carbonate (EC)/diethyl carbonate (DEC) (volume ratio of 1 : 1) (received from Tomiyama pure chemical industries LTD).

The beaker-type cells were applied for *ex-situ* XRD and XANES measurements. In the case of the *ex-situ* XRD measurement, a working electrodes were fabricated similarly as CR2032 coin-type cell, whereas the samples for the *ex-situ* XANES measurement were prepared by mixing of 5 wt% polytetrafluoroethylene (PTFE) binder, 30 wt% acetylene black (conductive agent), and 65 wt% active material of $Mn_{0.6}Mo_{1.2}V_{1.2}O_6$. Li foil was used as the counter and reference electrodes. Ni mesh (100 mesh Niraco) was selected as a current collector for the counter and the reference electrodes. 1 M $LiClO_4$ in EC/DEC was also used as electrolyte.

All the cell assembling (Li|1 M $LiClO_4$ in EC/DEC|$Mn_{1-x}Mo_{2x}V_{2(1-x)}O_6$ ($x = 0$, 0.4)) was performed in a glove box filled with argon gas. The charge–discharge measurement was carried out under galvanostatic conditions at various current densities at room temperature. Relaxation time between charge and discharge was set at 20 minutes. In the case of the *ex-situ* XRD measurement, the electrode was removed after the first lithium insertion–extraction, and then covered with polyethylene film to prevent the reaction with moisture in the air. The sample for the *ex-situ* XANES measurement was prepared potentiostatically. In this case, the electrode after lithiation was removed from the cell and evacuated for drying. Then, the sample was dispersed into boron nitride powder and pressed into a pellet. This pellet was sealed in a polyethylene bag filled with argon gas and used in the XANES measurement.

Results and discussion

Fig. 1(a) and (b) show the measured XRD patterns of $Mn_{1-x}Mo_{2x}V_{2(1-x)}O_6$ ($x = 0$, 0.4). The XRD patterns of both samples are identified as a monoclinic lattice. All the Bragg peaks are indexed to proper miller indices of a brannerite type structure without any impurity phase and match the JCPDS data (card number 35-139 for MnV_2O_6, 35-140 for $Mn_{0.6}Mo_{0.8}V_{1.2}O_6$).[13] Fig. 2 shows the crystal structure of brannerite MnV_2O_6. The brannerite structure is composed of VO_6 octahedra, which are connected to each other forming anion sheets parallel to the (001) planes.[17] Mn ions are situated between the oxygen sheets. This structure provides rather open spaces between the VO_6 sheets and forms a layered crystal structure, which is suitable for lithium insertion or extraction. Each lattice parameter of a, b, c and β for $Mn_{1-x}Mo_{2x}V_{2(1-x)}O_6$ ($x = 0$, 0.4) is summarized in Table 1. These values are consistent with the previous report.[13]

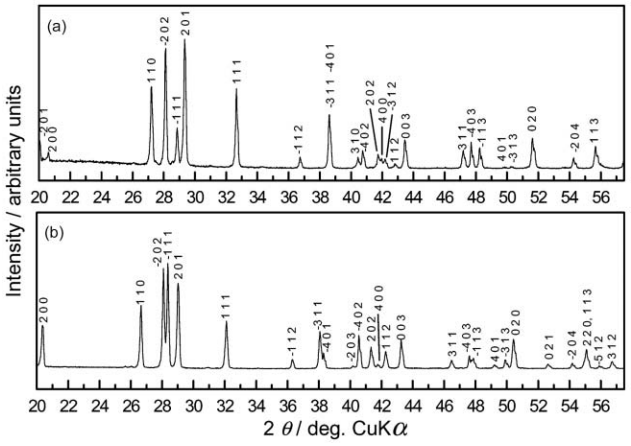

Fig. 1 XRD patterns of (a) MnV_2O_6 and (b) $Mn_{0.6}Mo_{0.8}V_{1.2}O_6$.

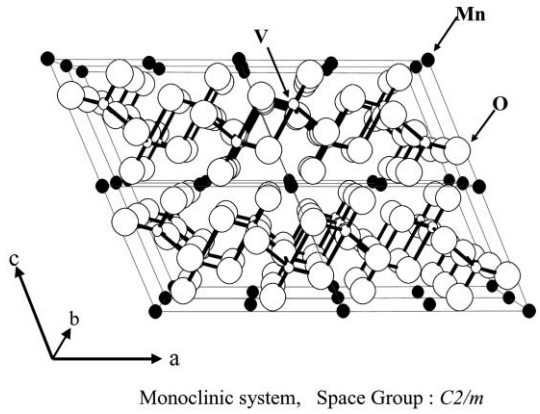

Fig. 2 Crystal structure of MnV_2O_6.

Table 1 Lattice parameters of $Mn_{1-x}Mo_{2x}V_{2(1-x)}O_6$ ($x = 0$, 0.4)

	a/Å	b/Å	c/Å	β/deg.
$Mn_{1-x}Mo_{2x}V_{2(1-x)}O_6$ ($x = 0$)	9.331(7)	3.541(1)	6.761(2)	112.5(1)
$Mn_{1-x}Mo_{2x}V_{2(1-x)}O_6$ ($x = 0.4$)	9.398(4)	3.618(1)	6.772(1)	112.1(6)

In order to investigate the oxidation states of Mn, V and Mo in the compounds, L-edge XANES measurements of Mn, V and Mo for synthesized samples $Mn_{1-x}Mo_{2x}V_{2(1-x)}O_6$ ($x = 0$, 0.4) were carried out. Fig. 3 shows the Mn L-edge XANES spectra of $Mn_{1-x}Mo_{2x}V_{2(1-x)}O_6$ ($x = 0$, 0.4) together with those of $MnCO_3$ (Mn^{2+}) and Mn_2O_3 (Mn^{3+}) as references. The spectra show strong absorption features due to the spin-orbit splitting of the Mn 2p core hole around 640–645 eV, and they correspond to the transition from the $Mn2p^63d^n$ to the $Mn2p^53d^{n+1}$ orbital. Mn L_{III} absorption peaks of $MnCO_3$ and Mn_2O_3 appear at about 642 eV and 643 eV, respectively. This result indicates that the Mn L_{III} absorption edge shifts to higher energy with increasing oxidation state of manganese.[14] Both synthesized MnV_2O_6 and $Mn_{0.6}Mo_{0.8}V_{1.2}O_6$ exhibit the same spectral features. Since the spectra of the edge jumps both for $MnCO_3$ and $Mn_{1-x}Mo_{2x}V_{2(1-x)}O_6$ ($x = 0$, 0.4) are very close to each other, Mn ions are present as close to Mn^{2+} in $Mn_{1-x}Mo_{2x}V_{2(1-x)}O_6$ ($x = 0$, 0.4) compounds. However, small peaks, which correspond to Mn^{3+}, are observed around 643 eV. Accordingly, a small amount of Mn^{3+} besides the main Mn^{2+}

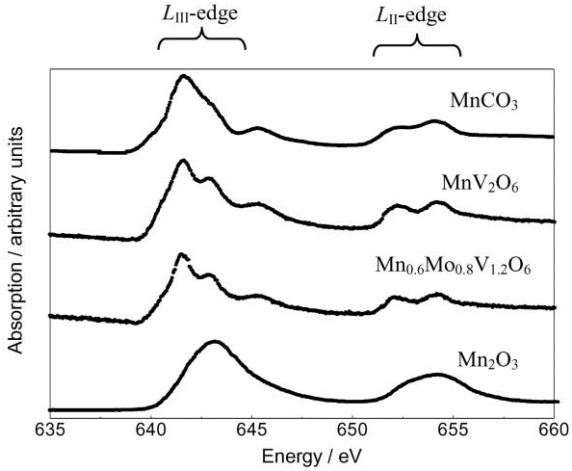

Fig. 3 Mn L-edge XANES spectra for $Mn_{1-x}Mo_{2x}V_{2(1-x)}O_6$ ($x = 0$, 0.4), $MnCO_3$ and Mn_2O_3.

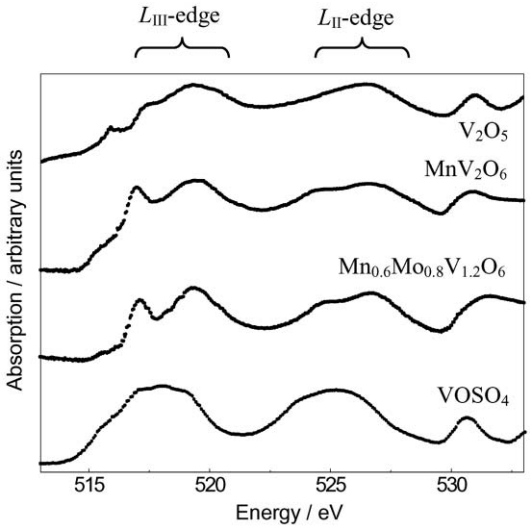

Fig. 4 V *L*-edge XANES spectra for $Mn_{1-x}Mo_{2x}V_{2(1-x)}O_6$ ($x = 0$, 0.4), V_2O_5 and $VOSO_4$.

may include in the solid solution $Mn_{1-x}Mo_{2x}V_{2(1-x)}O_6$ ($x = 0$, 0.4).

V *L*-edge XANES spectra of V_2O_5 (V^{5+}), $VOSO_4$ (V^{4+}) and $Mn_{1-x}Mo_{2x}V_{2(1-x)}O_6$ ($x = 0$, 0.4) in Fig. 4 illustrate that the valence of V in $Mn_{1-x}Mo_{2x}V_{2(1-x)}O_6$ ($x = 0$, 0.4) would be +5, because of the similar profile of $Mn_{1-x}Mo_{2x}V_{2(1-x)}O_6$ ($x = 0$, 0.4) and V_2O_5.

In the same way, Mo L_{III}-edge spectra of MoO_3 (Mo^{6+}), MoO_2 (Mo^{4+}) and $Mn_{0.6}Mo_{0.8}V_{1.2}O_6$ in Fig. 5 indicate that the oxidation state of Mo is +6 in $Mn_{0.6}Mo_{0.8}V_{1.2}O_6$. In the absorption of the Mo L_{III}-edge of MoO_3 and $Mn_{0.6}Mo_{0.8}V_{1.2}O_6$, the spectra split into two peaks due to splitting of a d-orbital. In pseudo-octahedral coordination, the first peak (t_{2g}) dominates, while in pseudo-tetrahedral coordination, the second peak (t_2) dominates.[18] Consequently, Mo is coordinated pseudo-octahedrally by oxide ions in $Mn_{0.6}Mo_{0.8}V_{1.2}O_6$ with brannerite structure.

In order to investigate the electrochemical performance of $Mn_{1-x}Mo_{2x}V_{2(1-x)}O_6$ ($x = 0$, 0.4), the cells were subjected to charge–discharge cycles at a constant current mode of 0.2 C (1 C = 350 A kg^{-1} of active material). Cutoff voltages were set at 0.01 V and 2.50 V. Fig. 6 shows the charge–discharge profiles of $Mn_{1-x}Mo_{2x}V_{2(1-x)}O_6$ ($x = 0$, 0.4) in the first and the second cycle. The insertion process of Li into the active materials is defined as the charge process, while the reverse holds for the extraction process. The profiles in the figure indicate that the first Li insertion in MnV_2O_6 shows a large

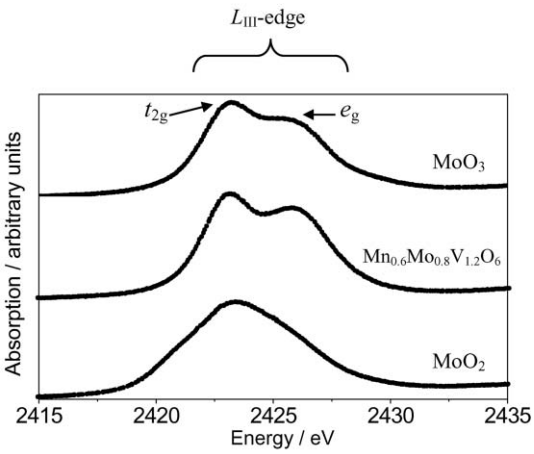

Fig. 5 Mo *L*-edge XANES spectra for $Mn_{0.6}Mo_{0.8}V_{1.2}O_6$, MoO_2 and MoO_3.

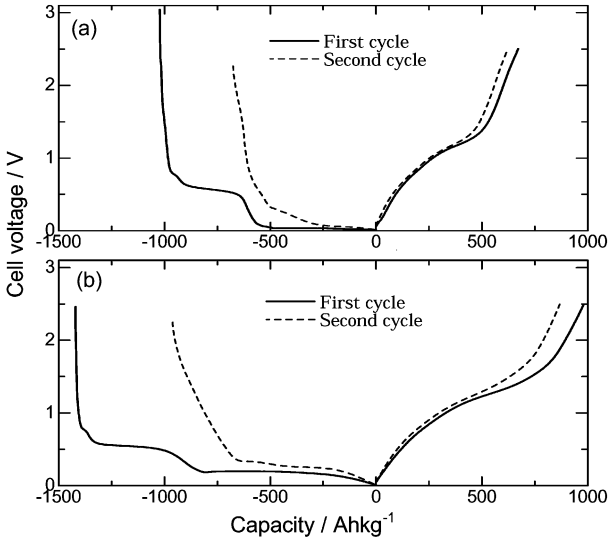

Fig. 6 The first and second charge–discharge curves of (a) MnV_2O_6 and (b) $Mn_{0.6}Mo_{0.8}V_{1.2}O_6$.

capacity of about 1000 Ah kg^{-1} and that of $Mn_{0.6}Mo_{0.8}V_{1.2}O_6$ is about 1400 Ah kg^{-1}, these capacities are much larger than that of graphite (about 350 Ah kg^{-1}). Furthermore, $Mn_{0.6}Mo_{0.8}V_{1.2}O_6$ has larger charge–discharge capacity than MnV_2O_6.

The first Li insertion profile of Mo doped brannerite $Mn_{0.6}Mo_{0.8}V_{1.2}O_6$ resembles that of the undoped MnV_2O_6 compound, because both compounds have three plateau regions during the first charge. $Mn_{0.6}Mo_{0.8}V_{1.2}O_6$ has plateaus around 0.7 V, 0.5 V and 0.2 V, and MnV_2O_6 has them around 0.7 V, 0.5 V and 0.05 V. Hereafter, the plateaus of highest voltage, middle voltage and lowest voltage are defined as the first, the second and the third plateau, respectively. This similarity in charge–discharge profile indicates that both brannerites (MnV_2O_6 and $Mn_{0.6}Mo_{0.8}V_{1.2}O_6$) have the similar mechanism of initial lithium insertion into the materials. However, the reason for the dissimilarities about the voltage, which is observed in the third plateau of MnV_2O_6 and $Mn_{0.6}Mo_{0.8}V_{1.2}O_6$, is not well interpreted at present.

The first and the second plateau in the first lithium intercalation process of both brannerites $Mn_{1-x}Mo_{2x}V_{2(1-x)}O_6$ ($x = 0$, 0.4) are not observed in the subsequent cycles. These results are indicative of the different mechanism of insertion of Li ions into $Mn_{1-x}Mo_{2x}V_{2(1-x)}O_6$ ($x = 0$, 0.4) between the first and the next cycles. In order to investigate the difference between the first and following cycles, *ex-situ* XRD measurement was examined for $Mn_{0.6}Mo_{0.8}V_{1.2}O_6$. The *ex-situ* XRD patterns of the electrode at the first charge (0.01 V) and at the discharge (2.50 V) including that of before electrochemical measurement are shown in Fig. 7. The peaks indicated by the solid circle originate from the polyethylene film, whereas the peak labeled with a solid square symbol is that of copper foil which is used as a current collector of the electrode. The principal peaks of the brannerite structure are observed clearly in the electrode before electrochemical measurement. However, these peaks disappear completely after the first charge (0.01 V), and they do not appear again after the subsequent discharge (2.50 V). It indicates that the $Mn_{0.6}Mo_{0.8}V_{1.2}O_6$ structure is transformed irreversibly from the crystalline to the amorphous phase during the first Li insertion. In the case of Li_xMVO_4 (M = Ni, Co, Zn, Cd) compounds, Guyomard *et al.*[19] also reported similar difference of the profiles between the first and subsequent cycles, they explained that it was due to the formation of a new type of amorphous lithiated material.

To evaluate the origin of irreversible capacity, cutoff voltages of the first charge were set at 0.65, 0.50, 0.25, 0.15

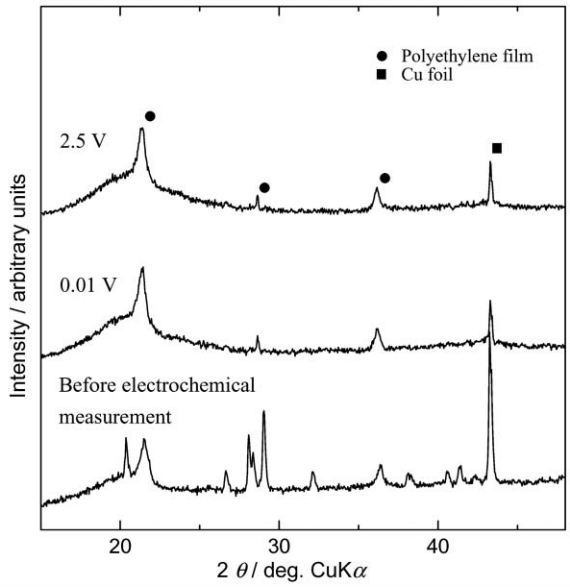

Fig. 7 *Ex-situ* XRD patterns of $Mn_{0.6}Mo_{0.8}V_{1.2}O_6$ at various voltages during the first cycle.

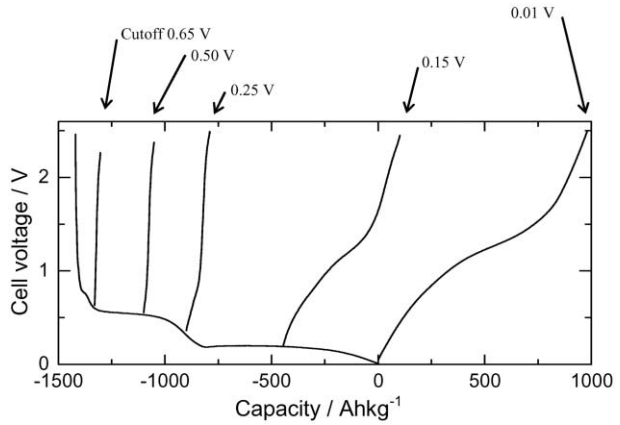

Fig. 8 The charge–discharge curves of $Mn_{0.6}Mo_{0.8}V_{1.2}O_6$ at various cutoff voltages.

and 0.01 V of $Mn_{0.6}Mo_{0.8}V_{1.2}O_6$ cell as is shown in Fig. 8. Discharge capacities at cutoff voltage from 0.65 to 0.50 V are almost zero. This means that either inserted Li ion at 0.50 V cannot be extracted from the active material, or it is irreversibly consumed for the reduction of electrolyte to form a solid electrolyte interface (SEI). On the other hand, a large discharge capacity was observed in the case of 0.15 or 0.01 V cutoff voltages. The large reversible capacity arises from the third plateau, and the third plateau has almost the same Li extraction capacity of discharge up to 2.5 V. Therefore, the larger Li extraction capacity of $Mn_{0.6}Mo_{0.8}V_{1.2}O_6$ than that of MnV_2O_6 is due to the larger capacity of the third plateau than that of the non-substituted brannerite.

In order to investigate the reaction mechanism of brannerite with a large amount of lithium, the oxidation states of each transition metal in the $Mn_{0.6}Mo_{0.8}V_{1.2}O_6$ electrode are considered from Mn, V and Mo *K*-edge XANES spectra at several voltages during the first charge. Fig. 9, 10 and 11 show the spectra for Mn, V and Mo in the electrode, respectively, together with reference materials that have various oxidation states. It is clear that the oxidation states of V and Mo in the electrodes before electrochemical measurements are +5 and +6, respectively, comparing with the reference compounds in Fig. 10 and 11. Mn exists as mainly +2 in Fig. 9. These results correspond to the *L*-edge XANES measurements for each

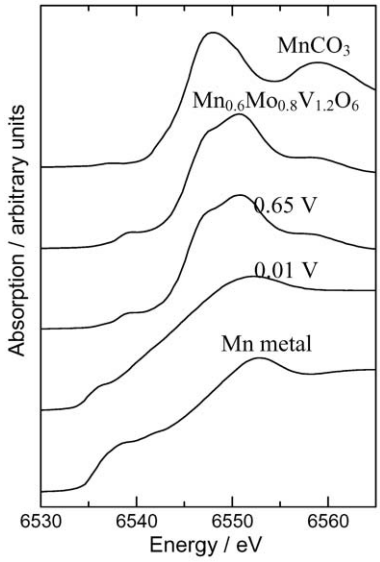

Fig. 9 Mn *K*-edge XANES spectra of the electrodes at various voltages.

transition metal as mentioned previously in Fig. 3, 4 and 5. When the electrode is fully lithiated up to 0.01 V, Mn and Mo exist as Mn^0 and Mo^0, respectively as shown in Fig. 9 and 11. V is +2 at this voltage, since the edge jump of the spectra is located between V metal and V_2O_3 (see Fig. 10). From the change in the oxidation state of all transition metals in the electrode, it is calculated that they can compensate only 9.6 Li per mol of $Mn_{0.6}Mo_{0.8}V_{1.2}O_6$. This compensation for Li ions is not enough to explain the total capacity of the initial charge, which is 14.1 Li per mol of $Mn_{0.6}Mo_{0.8}V_{1.2}O_6$, because one Li corresponds to a capacity of 100.4 Ah kg^{-1}. The possible explanations that can be drawn for the missing Li are 1) forming alloys between Li and transition metals, 2) formation of Li_2O and 3) consumption by SEI formation. In Fig. 7, no XRD patterns of metallic Mn, Mo and alloys of transition metals with Li are observed at 0.01 V of the electrode. Furthermore, we have reported previously about the strong ionic character of Li in the fully lithiated electrode of MnV_2O_6[12] by ^{7}Li NMR measurement. Therefore, these results suggest that neither deposition of transition metals nor alloying

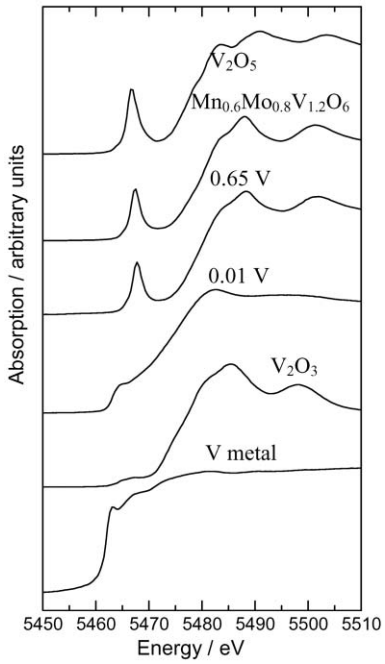

Fig. 10 V *K*-edge XANES spectra of the electrodes at various voltages.

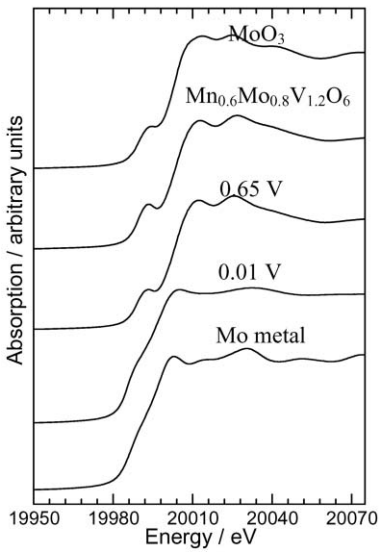

Fig. 11 Mo *K*-edge XANES spectra of the electrodes at various voltages.

of Li with transition metals occur. As to Li_2O formation, it is not clear until now, since it is difficult to detect Li_2O. Furthermore, in the case of the charged electrode at 0.65 V, which corresponds to the end of the first plateau during the first charge, Mn, V and Mo *K*-edge XANES spectra do not show any remarkable reductions compared with the electrode before electrochemical measurement. Therefore, the Li would be partially consumed by SEI formation during the initial lithiation which leads to the irreversible capacity, as previously shown in Fig. 8. In order to consider the excess amount of Li during the first charge, we quote the report about the charge compensation by both cobalt and nitrogen in $Li_{1.0}Co_{0.4}N$ from EELS measurement.[9] The other study of the oxide compounds RVO_4 (R = In, Ce, Fe, Al, Y)[20] suggests also that oxygen acts as a redox center leading to formation of "Li–O bond" thereby enhancing the capacity. We assume a similar mechanism, as mentioned above, to understand the large capacities of $Mn_{0.6}Mo_{0.8}V_{1.2}O_6$. Accordingly, it can be stated that the oxygen ions present in the $Mn_{0.6}Mo_{0.8}V_{1.2}O_6$ play an important role during the insertion and extraction of Li.

The charge and discharge capacities of $Mn_{1-x}Mo_{2x}V_{2(1-x)}O_6$ ($x = 0$, 0.4) *versus* cycle number are shown in Fig. 12. From the plots in the figure, it is clear that $Mn_{0.6}Mo_{0.8}V_{1.2}O_6$ has a larger charge and discharge capacity than that of MnV_2O_6 even after 9 cycles. Coulomb efficiencies are calculated from the cycle performance of $Mn_{1-x}Mo_{2x}V_{2(1-x)}O_6$ ($x = 0$, 0.4) at each cycle as depicted in Fig. 13. Both brannerites exhibit a higher coulomb efficiency, more than 90%, after second cycle.

The charge–discharge profiles for each brannerite *versus* current density with 0.1 C and 1.5 C are shown in Fig. 14. The

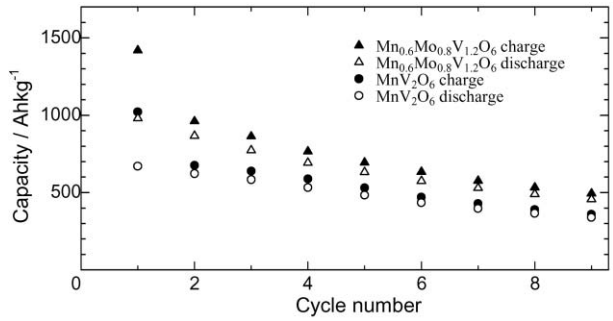

Fig. 12 The variation of charge-discharge capacities of $Mn_{1-x}Mo_{2x}V_{2(1-x)}O_6$ ($x = 0$, 0.4) *versus* cycle number.

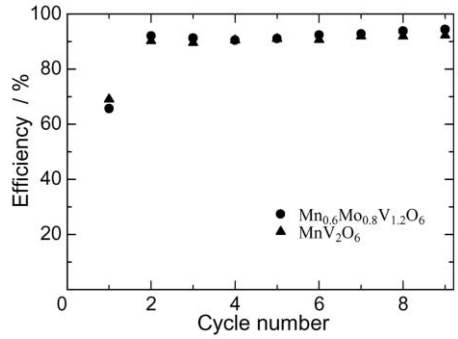

Fig. 13 The variation of coulomb efficiency of $Mn_{1-x}Mo_{2x}V_{2(1-x)}O_6$ ($x = 0$, 0.4) *versus* cycle number.

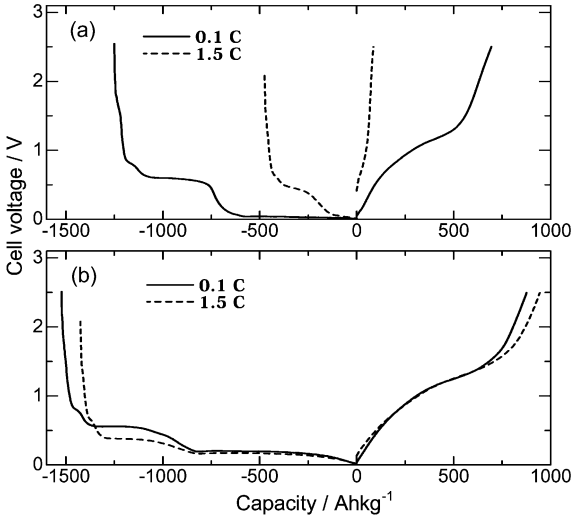

Fig. 14 The variation of charge–discharge curves of (a) MnV_2O_6 and (b) $Mn_{0.6}Mo_{0.8}V_{1.2}O_6$ with current density.

charge and discharge capacities for $Mn_{0.6}Mo_{0.8}V_{1.2}O_6$ do not exhibit any remarkable difference between 0.1 C and 1.5 C, whereas in the case of MnV_2O_6, the large capacity fade at 1.5 C is observed compared with that of 0.1 C. One of the reasons to explain this phenomenon is the overpotential, which may reduce the capacity of the third plateau in MnV_2O_6.

Fig. 15 shows the variations of the first charge and discharge capacities with various current densities for $Mn_{1-x}Mo_{2x}V_{2(1-x)}O_6$ ($x = 0$, 0.4). As is already shown in Fg. 14(a), a large capacity fade for MnV_2O_6 is observed with increasing current density, whereas that of $Mn_{0.6}Mo_{0.8}V_{1.2}O_6$ is small.

To clarify the difference of the rate performance, the

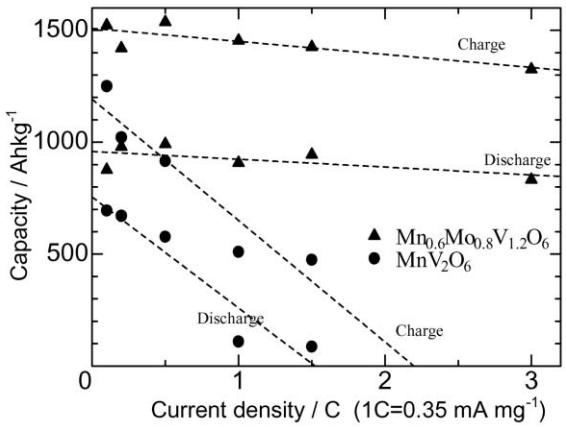

Fig. 15 The variation of charge-discharge capacity of $Mn_{1-x}Mo_{2x}V_{2(1-x)}O_6$ ($x = 0$, 0.4) with current density.

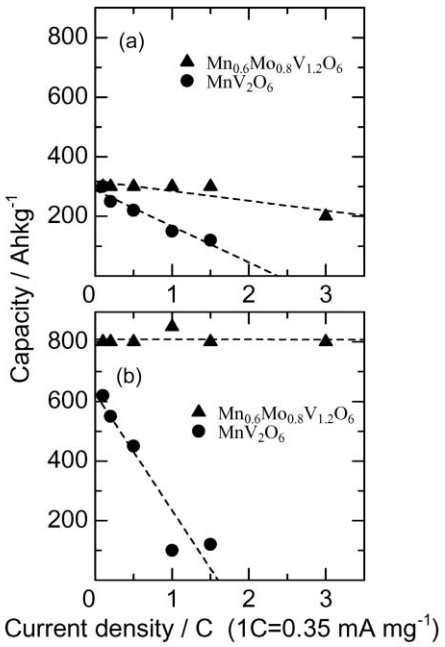

Fig. 16 The variation of the capacity of the (a) second and (b) third plateaus during the first charge of $Mn_{1-x}Mo_{2x}V_{2(1-x)}O_6$ ($x = 0$, 0.4) with current density.

variations of capacity of the second and the third plateaus are depicted in Fig. 16(a) and (b), respectively. As is shown in this figure, the rate performance of Mo doped sample is better than that of undoped sample in the both second and the third plateau regions. Although there are many factors such as charge transfer, electrode surface resistance *etc.*, generally it is said that ion diffusion is a rate-determining factor of the materials in a charge–discharge process. In the case of $Mn_{0.6}Mo_{0.8}V_{1.2}O_6$ before electrochemical measurement, vacancies are introduced in Mn site by the Mo doping. Even after amorphization during the first charge, we consider that the local structure reflects the initial structure of brannerite, because neither metallic deposition of transition metals nor alloys with Li are observed as mentioned above. Furthermore, all the capacity at each plateau decreases with the current density, it is natural to understand that the Li ion diffusion affects mostly the rate performance. Therefore, since vacancies would facilitate the lithium ion diffusion, the Mo doped sample has a better rate performance than the undoped one.

Conclusions

$Mn_{1-x}Mo_{2x}V_{2(1-x)}O_6$ ($x = 0$, 0.4) synthesized by classical solid state reaction had a brannerite type structure. The oxidation states of V and Mo in $Mn_{1-x}Mo_{2x}V_{2(1-x)}O_6$ were +5 and +6, respectively, whereas Mn had a mixed valence of +2 and +3, mainly +2.

The investigation of the electrochemical performance indicated that $Mn_{1-x}Mo_{2x}V_{2(1-x)}O_6$ ($x = 0$, 0.4) compounds had larger reversible capacity values than graphite. These two compounds with the brannerite type structure transformed irreversibly to an amorphous phase during the first lithiation. Furthermore, Mo doped brannerite $Mn_{0.6}Mo_{0.8}V_{1.2}O_6$ had a larger reversible capacity than the parent brannerite MnV_2O_6. The Mo doped compound showed a better rate property than the parent MnV_2O_6.

Acknowledgement

This work was supported by a Grant-in-Aid for Scientific Research on Priority Areas (B) (No. 740) ''Fundamental Studies for Fabrication of All Solid State Ionic Devices'' from the Ministry of Education, Culture, Sports, Science and Technology.

References

1 M. Wakihara and O. Yamamoto, *Lithium Ion Batteries Fundamentals and Performance*, Kodansha, Tokyo, 1998, p. 1.
2 M. Wakihara, *Mater. Sci. Eng.*, 2001, **R33**, 109.
3 P. Yu, B. N. Popov, J. A. Ritter and R. E. White, *J. Electrochem. Soc.*, 1997, **146**(1), 8.
4 M. G. S. R. Thomas, P. G. Bruce and J. B. Goodenough, *Solid State Ionics*, 1985, **17**, 13.
5 M. Wakihara, L. Guohua, H. Ikuta and T. Uchida, *Solid State Ionics*, 1996, **86–88**, 907.
6 C. Rossignol and G. Ouvrard, *J. Power Sources*, 2001, **97–98**, 491.
7 S. Denis, E. Baudrin, F. Orsini, G. Ouvrard, M. Touboul and J.-M. Tarascon, *J. Power Sources*, 1999, **81–82**, 79.
8 M. Nishijima, T. Kagohashi, Y. Takeda, M. Imanishi and O. Yamoto, *J. Power Sources*, 1997, **68**, 510.
9 T. Shodai, Y. Sakurai and T. Suzuki, *Solid State Ionics*, 1999, **122**, 85.
10 H. Kim, Y.-J. Kim, D. G. Kim, H.-J. Sohn and T. Kang, *Solid State Ionics*, 2001, **144**, 41.
11 M. Winter and J. O. Besenhard, *Electrochim. Acta*, 1999, **45**, 31.
12 S.-S. Kim, H. Ikuta and M. Wakihara, *Solid State Ionics*, 2001, **139**, 57.
13 R. Kozlowski, J. Ziolkowski, K. Mocala and J. Haber, *J. Solid State Chem.*, 1980, **35**, 1.
14 J. Kawai, Y. Mizutani, T. Sugimura, M. Sai, T. Higuchi, Y. Harada, Y. Ishiwata, A. Fukushima, M. Fujisawa, M. Watanabe, K. Maeda, S. Shin and Y. Gohshi, *Spectrochim. Acta, Part B*, 2001, **55**, 1385.
15 C. M. Kim, B. D. DeVries, B. Fruhberer and J. G. Chen, *Surf. Sci.*, 1995, **327**, 81.
16 S.-S. Kim, S. Ogura, H. Ikuta, Y. Uchimoto and M. Wakihara, *Solid State Ionics*, 2002, **146**, 249.
17 K. Mocala and J. Ziolkowski, *J. Solid State Chem.*, 1987, **69**, 299.
18 J. A. Rodriguez, J. C. Hanson, S. Chaturvedi, A. Maiti and J. L. Brito, *J. Phy. Chem. B*, 2000, **104**, 8145.
19 D. Guyomard, C. Sigala, A. G. L. Salle and Y. Piffard, *J. Power Sources*, 1997, **68**, 692.
20 S. Denis, E. Baudrin, M. Touboul and J.-M. Tarascon, *J. Electrochem. Soc.*, 1997, **144**, 4099.